Planar Hall Effect (PHE) Magnetometers

Vladislav Mor, Asaf Grosz and Lior Klein

Abstract The planar Hall effect (PHE) is intimately related to the anisotropic magnetoresistance (AMR). However, while AMR-based magnetic sensors have been commercially available for decades and are widely used in a variety of applications, PHE-based sensors have been mostly the subject of research. The reason for that is most probably the superior performance that has been exhibited by the AMR sensors. In this chapter, we review the work that has been done in the field of PHE sensors with emphasis on the PHE sensors developed by the authors. The performance of these sensors exceeds the performance of commercially available AMR-based sensors and has the potential of competing even with bulkier ultra-sensitive sensors such as flux-gate and atomic magnetometers. We review the physical origin of the effect, the use of shape to tailor the magnetic anisotropy on demand and the optimization process of the fabrication details of the sensor and its amplification circuit.

1 Physical Background

The interplay between spin polarized current and magnetic moments gives rise to many challenging and intriguing phenomena. The emergence of the field of spintronics [1, 2] highlighted phenomena encountered in heterostructures such as giant

---

V. Mor · L. Klein
Department of Physics, Nano-Magnetism Research Center, Institute of Nanotechnology and Advanced Materials, Bar-Ilan University, 52900 Ramat-Gan, Israel
e-mail: vladislav.mor@gmail.com

L. Klein
e-mail: Lior.Klein@biu.ac.il

A. Grosz (✉)
Department of Electrical and Computer Engineering, Ben-Gurion University of the Negev, P.O. Box 653, 84105 Beer-Sheva, Israel
e-mail: asaf.grosz@gmail.com

A. Grosz et al. (eds.), *High Sensitivity Magnetometers*, Smart Sensors, Measurement and Instrumentation 19, DOI 10.1007/978-3-319-34070-8_7

magnetoresistance, tunneling magnetoressitance, spin-torque, etc. Several additional important phenomena are encountered in a single compound, such as the dependence of the longitudinal resistivity ρ_{xx} and that of the transverse resistivity ρ_{xy} on the orientations of the current density J and the magnetization M. For polycrystalline magnetic conductors (including ferromagnetic *3d* alloys) the dependence is given by:

$$\rho_{xx} = \rho_{\perp} + \left(\rho_{\parallel} - \rho_{\perp}\right) \cos^2 \theta \tag{1}$$

$$\rho_{xy} = \frac{1}{2}\left(\rho_{\parallel} - \rho_{\perp}\right) \sin 2\theta \tag{2}$$

where $\rho_{\parallel}$ and $\rho_{\perp}$ are the resistivities for magnetization parallel and perpendicular to the current, respectively, and θ is the angle between J and M (see Fig. 1). The variation of ρ_{xx} is called the anisotropic magnetoresistance (AMR), while the variation of ρ_{xy} is called the planar Hall effect (PHE) [3, 4].

The AMR and PHE can be more complicated when the magnetic conductor is crystalline. In this case, in addition to the angle between J and M, the angles between each of the two vectors and the crystal axes may also be relevant, and the magnetotransport tensor ρ_{ij} is expressed as a function of the direction cosines, α_i, of the magnetization vector [5],

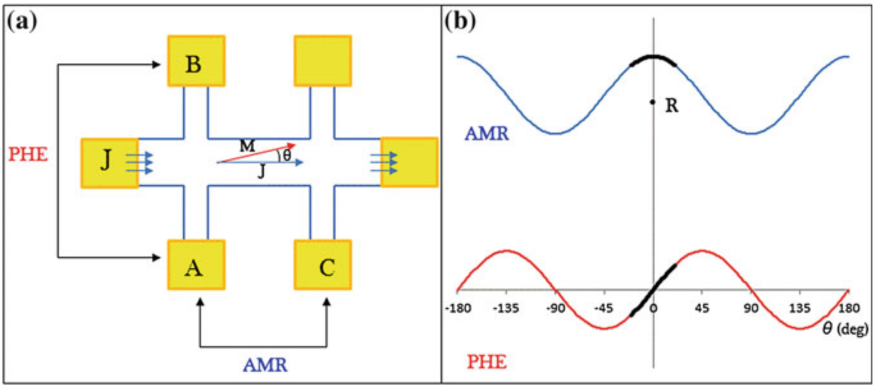

Fig. 1 **a** A sketch of a typical pattern used for measuring AMR and PHE. **b** The dependence of the longitudinal and transverse resistance on the angle θ between the current J and the magnetization M demonstrating AMR (*blue graph*) and PHE (*red graph*), respectively

$$\rho_{ij}(\alpha) = \sum_{k,l,m\ldots=1}^{3} \begin{pmatrix} a_{ij} + a_{kij}\alpha_k + a_{klij}\alpha_k\alpha_l + a_{klmij}\alpha_k\alpha_l\alpha_m \\ + a_{klmnij}\alpha_k\alpha_l\alpha_m\alpha_n + \cdots \end{pmatrix} \tag{3}$$

where *i, j* = *1,2,3* and the *a*'s are expansion coefficients. As usual, $\rho_{ij}(\alpha) = \rho_{ij}^s(\alpha) + \rho_{ij}^a(\alpha)$ where, ρ_{ij}^s and ρ_{ij}^a are symmetric and antisymmetric tensors, respectively. As the AMR and PHE are symmetric, only the symmetric part of the tensor is used to extract the AMR and PHE equations to replace Eqs. (1) and (2).

Theoretical treatment of AMR and PHE in *3d* itinerant ferromagnets has been mainly done in the framework of two channel *sd*—scattering model. In this model, conduction (carried primarily by *s* electrons) is divided into spin-up and spin-down currents which flow in parallel and mix via a spin-orbit interaction which depends on the angle between the *k* vector of the conduction electron and the orientation of the magnetic moments.

The AMR of *3d* magnetic alloys is on the order of several percent and their room temperature resistivity is on the order of 50 μΩ cm . Therefore, typically the PHE amplitude given by $(\rho_{\|} - \rho_{\perp})$ is on the order of 1 μΩ cm. For films with thickness on the order of 100 nm, the actually measured ΔR is on the order of 0.1 Ω.

Much larger PHE amplitudes are obtained in GaAs(Mn) [6], manganites [7], and magnetites [8], and for this reason the PHE in these compounds is termed giant. The origin of the giant PHE is not high AMR ratio but much larger ρ_{xx}.

2 PHE Sensors

The dependence of the PHE signal on the angle between the magnetization direction in the magnetic conductor and the direction of the current that flows through it is used for magnetic field sensing. For such a use the magnetic conductor should have uniform magnetization, and the magnetization direction should change predictably, reversibly and without hysteresis in the presence of an applied magnetic field. To obtain such a behavior, the layer should have magnetic anisotropy, commonly with an easy axis parallel to the current direction. When these conditions are met, the PHE signal indicates the magnetization direction which indicates the magnitude of the applied magnetic field in the film plane, in a perpendicular direction to the current direction.

In comparison with AMR sensors, PHE sensors have several intrinsic advantages. The AMR as a function of the angle θ between the current and the magnetization has its largest slope at $\frac{\pi}{4} + \frac{n\pi}{2}$ whereas the PHE as a function of θ has its largest slope at $\frac{n\pi}{2}$. Since it is easier to fabricate sensors where in the absence of an applied magnetic field θ is equal to $\frac{n\pi}{2}$ PHE sensors are simpler and cheaper to manufacture.

Furthermore, the AMR signal is measured on top of a large dc component associated with the average resistance (see Fig. 1b). Therefore, temperature and aging drifts which affect the dc component are extremely detrimental to AMR sensors. To obtain an output voltage which reflects the AMR signal without the dc component, AMR sensors are commonly used in a Wheatstone bridge configuration of four AMR sensors. Such a design is not needed in PHE sensors whose dc component is zero (see Fig. 1b).

Different types of PHE sensors have been reported:

1. Sensors with a single ferromagnetic layer with magnetic anisotropy which is induced during growth by applying a magnetic field and by using an antiferromagnetic pinning layer.
2. Sensors with multi ferromagnetic layers separated by non-magnetic conductors. These sensors are commonly called spin valve PHE sensors.
3. Sensors that are called PHE Bridge (PHEB) sensors but in fact are AMR sensors in a common Wheatstone bridge configuration.
4. Sensors with a single ferromagnetic layer and shape induced magnetic anisotropy due to their elliptical shape. This is the type of sensors with the best reported magnetic field resolution and we will elaborate on the properties of these sensors in the following sections.

2.1 PHE Sensors with Field Induced Magnetic Anisotropy

Uniform and reversible response of a sensing ferromagnetic layer in a PHE sensor has been obtained by inducing uniaxial magnetic anisotropy during growth. A common structure of such sensors consists of a ferromagnetic $Ni_{80}Fe_{20}$ layer coupled to an antiferromagnetic IrMn layer. A field on the order of several hundreds of Oersteds induces magnetic anisotropy and aligns the pinning direction of the IrMn layer [9–12].

2.2 Spin-Valve PHE Sensors

PHE sensors that consist of at least two ferromagnetic layers separated by non-magnetic layers are commonly called PHE sensors with spin-valve structure (Fig. 2). This term refers to the fact that such magnetic multilayer structures are used to obtain a spin-valve effect; namely, that for a given voltage the current flow is high or low depending on the relative orientation of the magnetization in neighboring magnetic layers (parallel or anti-parallel). Following are spin valve structures that are used to fabricate PHE sensors.

A common structure used for spin-valve PHE sensors is $Ta/Ni_{80}Fe_{20}/Cu/Ni_{80}Fe_{20}/IrMn/Ta$ [13–28]. The structure is commonly deposited on silicon dioxide in dc magnetron sputtering system. The first Ta layer is a seed layer, the

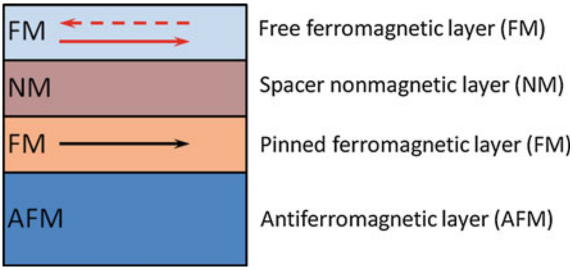

Fig. 2 A typical layer structure of a spin-valve PHE sensor

first $Ni_{80}Fe_{20}$ layer is the free magnetic layer, the Cu layer serves as the non-magnetic metallic spacer, the second $Ni_{80}Fe_{20}$ layer is the pinned ferromagnetic layer, the IrMn layer is an antiferromagnetic layers that pins the $Ni_{80}Fe_{20}$ layer below, and the second Ta layer is a capping layer.

The layers are commonly sputtered in a working pressure of several mTorr with a magnetic field on the order of several hundreds Oersted parallel to the film plane. The role of the field is to induce magnetic anisotropy in the ferromagnetic layers and define the exchange bias between the antiferromagnetic layer and the neighboring ferromagnetic layer. Typical thicknesses are: Ta—5 nm, free NiFe—4–20 nm, Cu—1–4 nm, pinned NiFe—1–12 nm, IrMn—10–20 nm.

A sensitivity of 15.6 mΩ/Oe was reported for a structure with free layer thickness of 20 nm and pinned layer thickness of 2 nm [29]. Other reports indicate sensitivity of less than 10 mΩ/Oe [16, 21, 24, 30]. Other spin valve structures include Co/Cu/Py [31–33], Co/Cu multilayers [34], NiFe/FeMn/NiFe [35], and Ta/NiFe/CoFe/Cu/CoFe/IrMn/Ta [14]. However, for these structures either sensitivity data are missing or the sensitivity is lower than for the Ta/$Ni_{80}Fe_{20}$/Cu/Ni80Fe20/IrMn/Ta structures.

In these sensors the spin valve structure is used to induce the required magnetic properties. There are no reports of additional transverse voltage in relation to the spin valve effect itself; namely, the large variations in the longitudinal resistivity as a function of the magnetic configuration. The measured PHE signal is simply the average contribution of all layers in connection with the AMR of each layer.

2.3 PHE Bridge Sensors

The term PHE bridge (PHEB) sensors [9–12, 24, 36–41] has been used to describe AMR sensors in different Wheatstone bridge configurations. Two main types have been considered: (a) sensors where the arms are straight and form a square; (b) sensors where the arms form a ring shape [42]. The two basic shapes have been further developed into meander-like shapes to increase the signal (see Fig. 3). In all these configurations at zero applied field the angle between the internal magnetization and the current is around 45° as required for AMR sensors and not parallel or anti-parallel as required for PHE sensors.

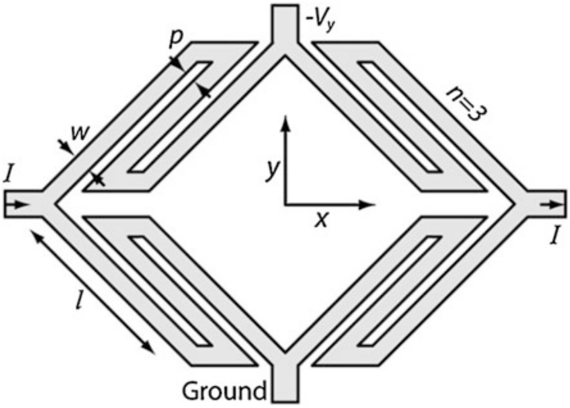

Fig. 3 Planar Hall effect Bridge (PHEB) configuration with multi segments per branch (*Source* Ref. [10])

The bridge configuration which is useful for eliminating effects of thermal drifts, and the angle between the current and the internal magnetization when no field is applied give rise to a dependence of the output voltage on the magnetization direction which is similar to that obtained for PHE; nevertheless, these are in fact AMR sensors whose output is determined by the integrated AMR response of the entire bridge structure. Such sensors have demonstrated a resolution of 2 nT/√Hz at 1 Hz [10].

3 Elliptical PHE Sensors

Starting from this section we concentrate on elliptical PHE sensors which exhibit magnetic field resolution of ~200 pT/√Hz at 1 Hz and less than 1 nT/√Hz at 0.1 Hz.

The elliptical shape of these sensors induces uniaxial magnetic anisotropy parallel to the long axis of the ellipse. For sensing, a current is driven along the long axis of the ellipse and the transverse voltage due to the PHE is measured across the short axis of the magnetic ellipse (see Fig. 4).

We start with describing the fabrication process and then we introduce the main factors which are used to analyze the operation of the sensor: the equivalent circuit, the signal and noise models and the resulting resolution.

3.1 Fabrication

The sensors are fabricated by the following steps:

1. We start with an undoped Si wafer (orientation: (100) ± 0.9°, resistivity $> 100\Omega\,\text{cm}$, micro roughness ≤ 5 Å).

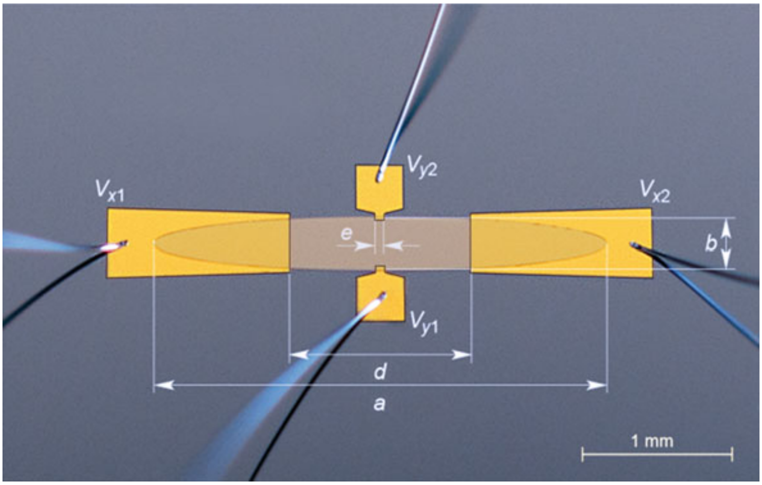

Fig. 4 An elliptical PHE sensor with its dimensions. The elliptical part is made of permalloy capped with tantalum. The current leads (V_{x1}, V_{x2}) and the voltage leads (V_{y1}, V_{y2}) are made of gold

2. Ellipses are patterned on the wafer by a liftoff process using MJB-4 Mask-aligner, photoresist S1813 and developer MICROPOSIT® MF®-319.
3. Permalloy ($Ni_{80}Fe_{20}$) films capped with tantalum are sputtered in a UHV-evaporation and sputtering system (BESTEC). Prior to deposition, the wafer is treated with Ar^+ beam using 3 cm dc Ion Source Filament Cathode (ITI) in order to remove resist and developer residue that can remain after development process. Base vacuum before deposition is less than 5×10^{-7} mBar, and it rises to 3×10^{-3} mBar during deposition. Gas is introduced into the upstream end of the ion source through the gas feed tube where it is ionized. The Permalloy is sputtered at a rate of $1.76\,\text{Å}/s$ and a capping layer of tantalumn (3 nm) is deposited on top in situ immediately after Permalloy to prevent oxidation.
4. The wafer is immersed in NMP for liftoff.
5. Current and voltage leads are patterned at a second liftoff process.
6. The gold contacts are sputtered on top of an adhesion layer of chrome (4 nm) in BESTEC. Before deposition the wafer is treated with Ar^+ beam. The gold layer thickness is ~ 1.5 times the thickness of the magnetic layer.
7. The wafer is immersed in NMP heated to 80 °C for liftoff.

The liftoff process described in (2), (3) and (4) can be replaced by a wet etching process. In this process the new stage (2) is former stage (3) performed on an unprocessed wafer. Stage (3) is former stage (2) with reversed lithography (namely the remaining photoresist defines the ellipses. Stage (4) is replaced by wet etching with 32 % HCl. The etching is stopped by H_2O.

3.2 Equivalent Circuit

The equivalent electrical circuit of the PHE sensor and its preamplifier is presented in Fig. 5. The equivalent circuit includes the PHE voltage source which generates a V_y voltage across the sensor y-terminals, the sensor resistance across the y-terminals, R_y, the sensor internal thermal and 1/*f* noise sources $e_{thermal}$ and $e_{1/f}$ respectively, and e_{amp}, the total preamplifier noise, referred to its input (including the voltage noise, current noise, and the noise of the feedback resistors R_f and R).

3.3 Signal

The sensitivity of a PHE sensor is defined as the ratio between the PHE voltage V_y and the magnetic field B applied in the film plane perpendicular to the easy axis (and the current direction). When B is small compared to the total effective anisotropy field (H_k) which is the sum of the sensor shape induced anisotropy H_{sa} and the excess anisotropy H_{ea}, the sensitivity can be expressed as follows [43]

$$S_y = \frac{V_y}{B} = 10^4 \frac{V_x}{R_x} \cdot \frac{\Delta\rho}{t} \cdot \frac{1}{H_{sa} + H_{ea}} \tag{4}$$

where V_x is the bias voltage across the x-terminals, R_x is the sensor resistance across the x-terminals, t is the sensor thickness, and $\Delta\rho$ is the sensor average electrical resistivity $(\Delta\rho = \rho_{\parallel} - \rho_{\perp})$.

We express the sensor resistance across the x-terminals R_x, while neglecting the resistance of the gold leads and the interface resistance between the leads and the sensor as:

$$R_x = \frac{C_1 \cdot \rho \cdot d}{t \cdot b} \tag{5}$$

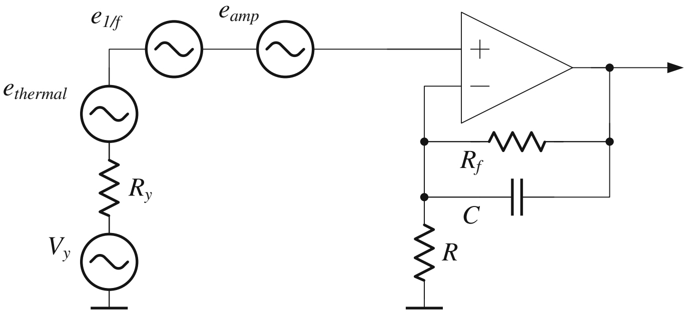

Fig. 5 Equivalent electrical circuit of the PHE sensor

In this expression, C_1 is a constant not much larger than 1 which is used to reflect the previously mentioned approximations.

3.4 *Noise*

The total noise of a PHE sensor e_Σ has three main components: 1/*f* noise, thermal noise, and preamplifier noise:

$$e_\Sigma = \sqrt{e_{1/f}^2 + e_{\text{thermal}}^2 + e_{amp}^2} \tag{6}$$

3.4.1 Thermal Noise

The thermal noise (sometimes referred to as Johnson noise) is generated by thermal agitation of electrons in a conductor and is defined by:

$$e_{\text{thermal}} = \sqrt{4k_B T R_y} \tag{7}$$

where k_B is the Boltzmann constant, T is the temperature, and R_y is the sensor resistance across the *y*-terminals:

$$R_y = \frac{C_3 \cdot \rho \cdot b}{t \cdot e \cdot C_2} \tag{8}$$

where C_3 similarly to C_1 is a constant not much larger than 1, and C_2 is a constant larger than 1 that relates the real, rectangle shaped volume between the *y*-terminals to the effective conduction area.

3.4.2 1/*f* Noise

The sensor 1/*f* noise is described using the Hooge empirical formula:

$$e_{1/f} = \sqrt{V_x^2 \frac{\delta_H}{N_c \cdot Vol \cdot f^\alpha}} \tag{9}$$

where V_x is the bias voltage, δ_H is the Hooge constant [44, 45], N_c is the "free" electron density and is equal to 1.7×10^{29} 1/m^3 for $Ni_{80}Fe_{20}$ Permalloy [45], *f* is the frequency, α is a constant, and *Vol* is the effective volume, where the electrons are contributing to the conduction process in a homogeneous sample [45].

Considering the effective conduction volume described using C_2 in Eq. (8), Vol can be approximated by:

$$Vol = C_2 \cdot t \cdot b \cdot e \tag{10}$$

3.4.3 Amplifier Noise

e_{amp} is the total preamplifier noise, referred to its input (including the voltage noise, current noise, and the noise of the resistors). The feedback resistors R_f and R are selected to be small enough so their noise contribution can be neglected. Consequently,

$$e_{amp} = \sqrt{v_{amp}^2 + \left(R_y i_{amp}\right)^2} \tag{11}$$

where v_{amp} and i_{amp} are the operational amplifier voltage and current noise respectively. The voltage and current noise of the operational amplifier possess both white and pink (1/*f*) noise components and can be expressed using the following expressions:

$$v_{amp} = v_{amp0}\sqrt{1 + \frac{f_{c1}}{f^{\alpha_1}}} \tag{12}$$

$$i_{amp} = i_{amp0}\sqrt{1 + \frac{f_{c2}}{f^{\alpha_2}}} \tag{13}$$

where v_{amp0} and i_{amp0} are the level of the voltage and current white noise densities respectively, f_{c1} and f_{c2} are the voltage and current noise densities corner frequency respectively and α_1 and α_2 are constants.

3.5 *Equivalent Magnetic Noise*

The sensor equivalent magnetic noise (sometimes referred to as resolution or minimal detectable field) is defined as

$$B_{eq} = \frac{e_\Sigma}{S_y} = \frac{\sqrt{e_{1/f}^2 + e_{\text{thermal}}^2 + e_{amp}^2}}{10^4 \frac{V_x}{R_x} \cdot \frac{\Delta\rho}{t} \cdot \frac{1}{H_{sa} + H_{ea}}} \tag{14}$$

In the following sections we describe a series of steps we have made to improve the magnetometer resolution with special emphasis on the low frequency noise.

4 Magnetic Behavior of Elliptical PHE Sensors

As mentioned above, the operation of PHE sensors requires magnetic anisotropy. In elliptical PHE sensors the magnetic anisotropy is induced by the dependence of the magnetostatic energy on the direction of the magnetization relative to the principal axes of the ellipse. Compared to previously discussed methods for the magnetic anisotropy induction (e.g. field induction or induction using an anti-ferromagnetic layer), anisotropy induction using the sensor shape has several important advantages:

1. The direction and magnitude of the magnetic anisotropy is determined by the pattern shape.
2. In principle, for ideal magnetic ellipsoids with no intrinsic magnetic anisotropy, the anisotropy field, which is inversely proportional to the signal [see Eq. (4)], can be made as small as required.
3. The anisotropy is achieved using a single magnetic layer which makes the fabrication simple. Furthermore, due to the fact that the anisotropy is not achieved via interaction with other layers, the magnetic sensing element can be as thick and big as required which is important for decreasing the 1/*f* noise.

For elongated and flat ellipsoids $(a \geq b \gg c)$, one can define and calculate the demagnetization factors [43, 46],

$$\frac{N_a}{4\pi} = \frac{c}{a}\left(1 - e^2\right)^{1/2}\frac{K - E}{e^2} \tag{15}$$

$$\frac{N_b}{4\pi} = \frac{c}{a}\frac{E - \left(1 - e^2\right)K}{e^2\left(1 - e^2\right)^{1/2}} \tag{16}$$

$$\frac{N_c}{4\pi} = 1 - \frac{cE}{a\left(1 - e^2\right)^{1/2}} \tag{17}$$

where *a, b* and *c* are the axes of the ellipsoid. N_a, N_b and N_c are the demagnetizing factors (corresponding to *a*, *b* and *c* respectively). *K* is a complete elliptic integral of the first kind and *E* is a complete elliptic integral of the second kind, whose argument is $e = \left(1 - \frac{b^2}{a^2}\right)^{\frac{1}{2}}$. The behavior of the ellipsoid when *H* is applied in the *ab* plane can be described by the Stoner-Wohlfarth Hamiltonian $\mathcal{H} = K_u \sin^2\theta - M_s H \cos(\alpha - \theta)$ [47] where the anisotropy constant K_u is given by $K_u = \frac{1}{2}M_s^2(N_b - N_a)$. So the shape-induced anisotropy field (H_{sa}) is

$$H_{sa} = M_s(M - L) \tag{18}$$

Using asymptotic expansions of K and E in the limit $a \gg b \gg c$ [46] we obtain

$$H_{sa} \sim 4\pi M_s \frac{c}{b} \sim 10,807 \frac{c}{b} Oe \tag{19}$$

Using this approximation we estimate the shape-induced anisotropy of a thin ellipse (thickness t) with principle axes a and b $(a \geq b \gg t)$ as

$$H_{sa} \sim 4\pi M_s \frac{t}{b} \sim 10,807 \frac{t}{b} Oe \tag{20}$$

As shown below, the effective anisotropy field does not go to zero when t/b goes to zero. Therefore, we denote by H_{sa} the calculated shape-induced anisotropy field and by H_k the actual effective anisotropy field.

The ideal magnetic ellipsoid is expected to exhibit a single magnetic domain behavior with uniform magnetization. Figures 6 and 7 present two types of experiments which demonstrate the effective single domain behavior of the thin ellipses.

Figure 6 demonstrates the effective single domain behavior by showing that if the magnetization is tilted away from the easy axis by an external field, it returns completely to the easy axis when the applied magnetic field is set to zero. This is demonstrated by measuring the PHE with and without the field. The small variations in the zero-field signals are consistent with the expected effect of a small ambient field.

Figure 7 shows the dependence of the switching Field H_s on α measured on elliptical sensor with long axis of 1 mm. The line is the expected for coherent rotation [47]

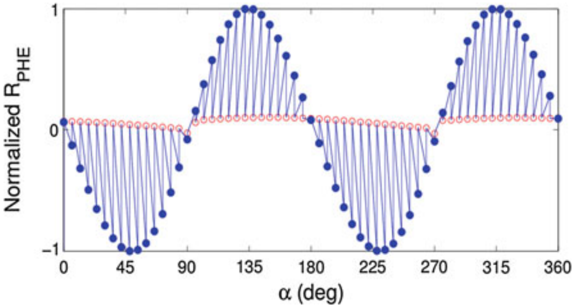

Fig. 6 Demonstration of effective single-domain behavior of large elliptical sensors. The normalized PHE is measured across an elliptical sensor as a function of the angle α between H and J. The dimensions of the ellipse are 2 mm length, 0.25 mm width, and 60 nm thickness, the current J is applied along the long axis of the ellipse. For each α, the voltage is measured twice: with H = 100 Oe (full symbols) and with H = 0 (empty symbols). (*Source* Ref. [43])

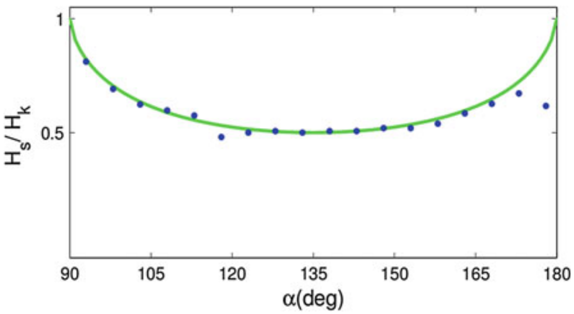

Fig. 7 The switching field H_s divided by the anisotropy field H_k as a function of α. The line is a fit to the Stoner–Wohlfarth model. The dimensions of the ellipse are 1 mm length, 0.125 mm width, and a 60 nm thickness. (*Source* Ref. [43])

$$H_s(\alpha) = \frac{H_k}{\left[\sin^{\frac{2}{3}}\alpha + \cos s^{\frac{2}{3}}\alpha\right]^{\frac{3}{2}}} \tag{21}$$

where H_k is the actual effective anisotropy field. We note that for α close to 180° the experimental points deviate from the theoretical prediction indicating that in this narrow range of angles the magnetization reversal cannot be described in terms of coherent rotation. This however does not affect the functionality of the sensors which are used to detect fields much smaller than the anisotropy field.

To determine the effective H_k of the sensors, we apply a small field perpendicular to the easy axis and measure the slope of θ versus $H_\perp$. Figure 8 represents the experimentally extracted H_k for elliptical sensors in a wide range of sizes as a function of b/t, where t is the film thickness, and b is the short axis of the ellipse.

We compare the analytical approximation with the experimental results (see Fig. 8) and note that the experimental value of H_k has a lower bound. Namely, there is an excess anisotropy which is sample dependent and its magnitude is typically on the order of 5 Oe. The origin of this excess anisotropy is yet to be determined. We

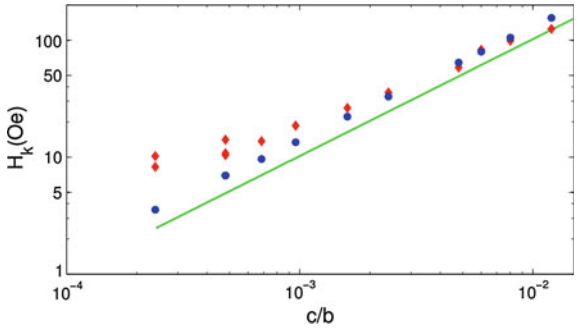

Fig. 8 The theoretical anisotropy field of ellipsoids with principle axes a, b and c [continuous line according to Eq. (19)] and the experimental (*diamonds*) and simulated (*dots*) shape anisotropy field for ellipses with principle axes a and b and thickness $t = c$ as a function of c/b. (*Source* Ref. [43])

therefore write H_k as a sum of two contributions: the expected anisotropy field due to shape denoted by H_{sa} and an excess anisotropy field denoted by H_{ea}.

We compare the analytical approximation with OOMMF [48] simulations and note that the approximation in Eq. (19) is quite good for $a/b \geq 8$.

We have also performed simulations for ellipses and rectangles and have found that the analytical approximation is better for elongated ellipses. The simulations also indicate the effective single domain behavior for ellipsoids and ellipses in a very wide range of sizes, whereas rectangular samples are much less stable. The ellipses with axes ratio of 6:1 and above behave quite like a single domain particle and the behavior improves with increasing axes ratio.

We note that the size dependence of the switching properties of Permalloy ($Ni_{80}Fe_{20}$) ellipses was also investigated by other groups using magnetoresistance measurements and magnetic force microscopy. A single-domain configuration was observed in the elements with the range of aspect ratios from 5 to 10. More complex domain structures appear in the lower aspect ratio and thicker samples [49].

Surprisingly, the single-domain-like behavior is observed even for very large ellipses [43]. This has a practical importance since the big ellipses have a very small H_k which means that their sensitivity can be higher.

$$S = \frac{V_y}{I} \cdot \frac{1}{H_k} \propto \frac{1}{H_k} \tag{22}$$

We have obtained H_k as small as 8 Oe and S as big as 200 $\frac{\Omega}{T}$.

5 Operation and Optimization of Elliptical PHE Sensors

5.1 Exciting the Sensor Using AC Current

As previously explained, the preamplifier consists of voltage and current noise sources at its input, both possessing white and 1/*f* components [see Eqs. (12) and (13)]. Our magnetometer is designed for optimal resolution at ultra-low frequencies starting from the mHz range. Since the 1/*f* noise of the elliptical PHE magnetometer is extremely low, even ultra-low noise operational amplifiers will introduce an additional, significant 1/*f* noise at frequencies below 1 Hz (see for example LT1028 by Linear Technology).

A probable solution is to use chopper or auto-zero amplifiers. Those amplifiers show minimal drift and zero 1/*f* noise at their input. However, even state-of-the-art commercially available amplifiers of this type (see for example ADA4528-1 by Analog Devices) demonstrate white noise levels five times higher compared to the white noise level of a standard ultra-low noise operational amplifier and therefore did not constitute a potential solution in this case.

To overcome this limitation we have excited our sensor using ac current as opposed to the classic approach of dc current excitation. Exciting the sensor using

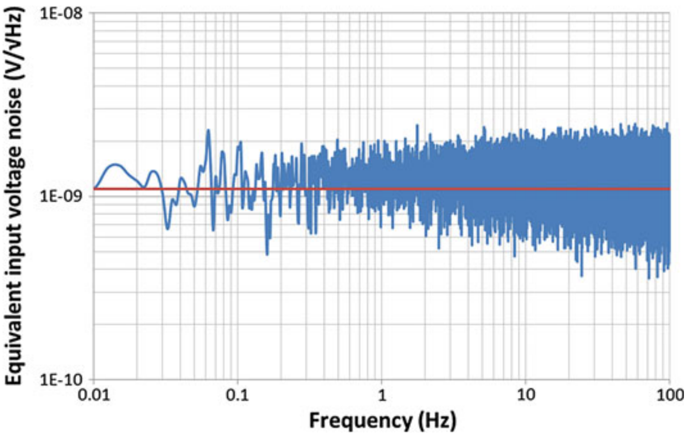

Fig. 9 Equivalent input voltage noise versus frequency for a LT1028 operational amplifier with an output demodulation at 1.12 kHz. Both the measured noise and the fit are shown (*blue* and *red line* respectively)

ac current translates its output signal and its intrinsic 1/*f* noise to frequencies where the 1/*f* noise of the preamplifier can be neglected. The preamplifier output signal can then be demodulated back to baseband using analog or digital synchronous detector.

Compared to chopper amplifiers which modulate the signal inside the amplifier, modulation of the signal inside the sensor itself results in an equivalent white noise behavior of the amplifier with a drastically lower noise level.

Figure 9 shows the amplitude spectral density of the LT1028 preamplifier equivalent input noise, measured after demodulation without excitation current. One can see that the preamplifier noise is white from 10 mHz to 100 Hz. The measured white noise level of $\sim$1.1 nV/$\sqrt{\text{Hz}}$ is in good agreement to the reported white noise level in the LT1028 op-amp datasheet. The graph in Fig. 9 was acquired using a digital demodulation at a frequency of 1.12 kHz.

5.2 *Optimization of the Sensor Thickness*

The PHE sensor 1/*f* noise is inversely proportional to the sensor volume [see Eq. (9)]. Since the sensor signal is inversely proportional to the sensor thickness, it is also inversely proportional to its volume [see Eq. (4)]. As a result, there is an optimal thickness for which the sensor equivalent magnetic noise is minimal.

Our magnetometer is optimized to operate at ultra-low frequencies where the 1/*f* noise component of the sensor is dominant over its thermal noise and the preamplifier white noise.

In the limit where the 1/*f* noise is dominant, only the first term under the square root of Eq. (6) remains relevant. The parameters $H_{ea}, \frac{\Delta\rho}{\rho}$, and ρ do not depend on the sensor thickness for $t > 20$ nm; therefore, they are considered as constants for the thicknesses we use. By substituting the expressions for H_{sa}, R_x, *Vol* and R_y into Eq. (14) we obtain:

$$B_{eq} = \sqrt{\frac{\delta_H}{N_c \cdot C_2 \cdot t \cdot b \cdot e \cdot f^{\alpha}} \frac{(10^4 t + b + H_{ea}) \cdot C_1 \cdot d \cdot \rho}{10^4 \cdot \Delta\rho \cdot b^2}} \tag{23}$$

We note that the equivalent magnetic noise in Eq. (23) depends only on the sensor dimensions and the material properties.

Optimizing t for minimal value of B_{eq} yields:

$$t_{opt} = \frac{H_{sa} \cdot b}{10^4} \tag{24}$$

We find that for this thickness:

$$H_{sa} \approx H_{ea} \tag{25}$$

We now substitute Eq. (24) into Eq. (23) and obtain the sensor low-frequency equivalent magnetic noise at the optimal thickness:

$$B_{\min} = \sqrt{\frac{\delta_H}{N_c \cdot C_2 \cdot e \cdot f^a} \frac{2\sqrt{H_{ea}} C_1 \cdot d \cdot \rho}{10^2 \cdot \Delta\rho \cdot b^2}} \tag{26}$$

To appreciate the sensitivity of B_{eq} on deviations from the optimal thickness, we calculate changes in B_{min} denoted as $B_{eq} = B_{min} \cdot \delta B_{eq}$ as a result of relative changes in the sensor thickness denoted as $\delta t = (t_{opt} \pm t)/t_{opt}$.

Fig. 10 Relative change in the equivalent noise as a result of deviations from the optimal thickness

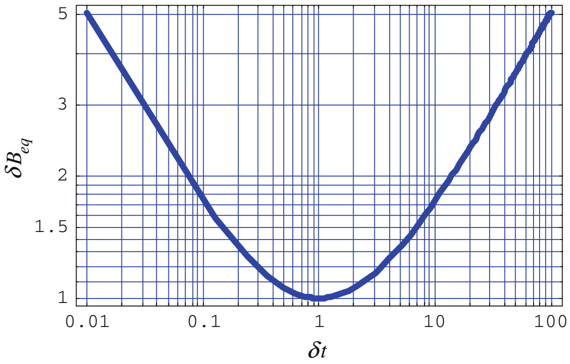

This yields

$$\delta B_{eq} = \frac{1}{2}(1 + \delta t)\sqrt{\frac{1}{\delta t}} \tag{27}$$

A plot of Eq. (27) (see Fig. 10) shows that a ten-fold deviation of the sensor thickness from its optimum value results in almost two-fold increase in the sensor equivalent magnetic noise.

5.3 Optimization of the Driving Current

Theoretically, if the sensor power consumption is not limited, the excitation current should be as high as possible to bring the equivalent magnetic noise to a minimum at all frequencies. However, the ability of the sensor to dissipate the excessive heat is limited and therefore, at a too high current, the sensor becomes thermally unstable, which degrades its equivalent magnetic noise.

The excitation current should be selected according to the bandwidth requirements of the specific application. In frequencies significantly higher or lower than 1 Hz, thermal or 1/*f* noise, respectively, will dominant over other noise sources regardless of the excitation current. On the other hand, the unique case of a bandwidth ranging from sub-Hz frequencies and up to tens or hundreds of Hz requires a more sophisticated approach for the selection of the excitation current based on an experimental optimization process.

In this case of intermediate frequencies the optimal current must yield best possible magnetic field resolution at frequencies where the 1/*f* noise dominants but also at frequencies where the white noise sources are dominant.

To find the optimal excitation current for the intermediate frequency range, we have measured the sensor equivalent magnetic noise between 0.01 and 10 Hz for currents in the range of 10–100 mA. We have changed the current by small steps

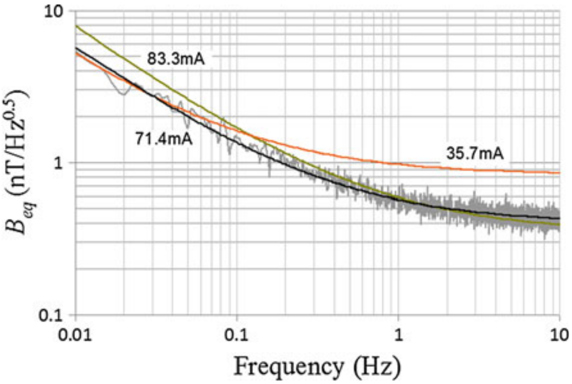

Fig. 11 Equivalent magnetic noise versus frequency. For the optimum excitation current amplitude of 71.4 mA, both the sensor noise and the noise fit are shown. For other excitation current amplitudes only the noise fits are shown. (*Source* [50])

measuring at each step the sensor gain and noise. Figure 11 shows the sensor equivalent magnetic noise as a function of frequency for three cases: a too high, a too low and optimal excitation current.

The sensor was excited with ac current. The sensor output was amplified using a low-noise operational amplifier (LT1028). The amplifier output was sampled by a 24-bit ADC (PXI-5421) and demodulated using a digital synchronous detector. A 100 Hz low-pass filter at the output of the synchronous detector was used to band-limit the signal. As the input voltage noise of the LT1028 operational amplifier flattens at around 1 kHz, we have excited the sensor at 1.22 kHz to avoid the amplifier 1/*f* noise and 50 Hz power network harmonics. The sensor gain was measured using a calibrated solenoid and was found to be flat from 10 mHz to 100 Hz. The sensor noise was measured inside a seven layer magnetic shield to suppress low-frequency interferences. A similar experimental setup is shown in Fig. 12. The experimental sensor parameters are listed in Table 1.

From Fig. 11, one can see that the sensor equivalent magnetic noise at the optimal excitation current is either the lowest one or does not practically differ from the noise values at the other excitation currents. A too low excitation current provides similar results at low frequencies but worse results at higher frequencies, where the 1/*f* noise is not so dominant. At a too high excitation current, the equivalent magnetic noise at high frequencies is similar to that of the optimal current, but is degraded at low frequencies due to thermal drift.

5.4 Equivalent Input Magnetic Noise

By increasing the sensor volume (see Fig. 13) and decreasing white noise associated with the pre-amplifier we have managed to considerably improve the equivalent magnetic noise of our PHE sensors and obtain a magnetic field resolution of 200 $\mathrm{pT}/\sqrt{\mathrm{Hz}}$ at 1 Hz and less than 1 $\mathrm{nT}/\sqrt{\mathrm{Hz}}$ at 0.1 Hz [51].

Figure 14 shows the 5 mm PHE sensor equivalent magnetic noise as a function of frequency compared to the equivalent magnetic noise of a high-resolution commercial AMR sensor of a model HMC1001 by Honeywell.

6 Future Prospects and Applications

The current resolution of the elliptical PHE-sensors exceeds the resolution of the highest performance commercial AMR sensors and the resolution of other MR sensors. However, there are prospects for improving the resolution of these sensors by more than an order of magnitude to reach field resolution in the femto-Tesla range. In the following we address several routes for improved resolution: (a) increasing the signal (b) increasing the measured field and (c) decreasing the noise.

There are two main ways to increase the signal. The AMR ratio of the used Permalloy films is on the order of 1–2 %. However, based on reports in the

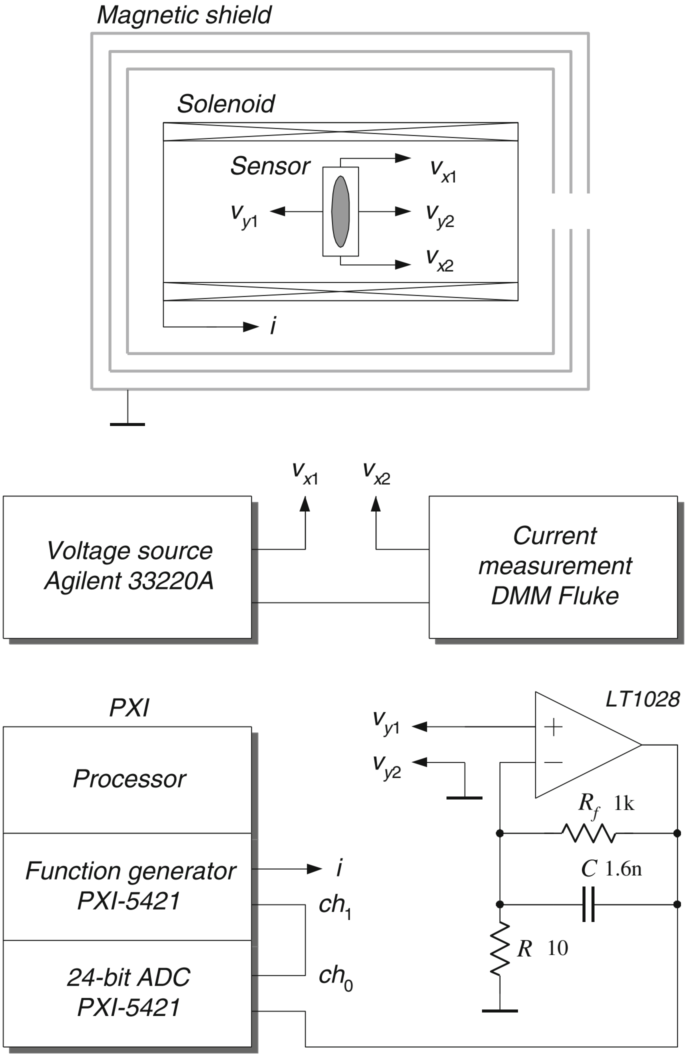

Fig. 12 An experimental setup similar to the one used for the excitation current optimization process. (*Source* Ref. [43])

literature, optimization of deposition conditions may reasonably yield an improvement of at least a factor of 2. We note that the equivalent magnetic noise is inversely proportional to the AMR ratio. Another way to increase the signal is by reducing the excess anisotropy H_{ex} which sets a lower bound for the total effective uniaxial anisotropy. The origin of the excess anisotropy is not fully understood at this stage. We believe that it is related to internal intrinsic magnetocrystalline anisotropy which can be suppressed by the optimization process of the growth

Table 1 Parameters of the PHE sensor experimental model

Parameter	Value	Units	Parameter	Value	Units
a	3	mm	H_a	3.84	Oe
b	0.375	mm	H_k	3.45	Oe
t	120	nm	$\Delta\rho/\rho$	1.6	%
d	1.2	mm	ρ	2.7×10^{-7}	Ohm m
e	0.06	mm	α	1.5	
R_x	9.97	Ohm	δH	2.73×10^{-3}	
R_y	5.08	Ohm	N_c	17×10^{28}	$1/\text{m}^3$
I_x	71.4	mA			

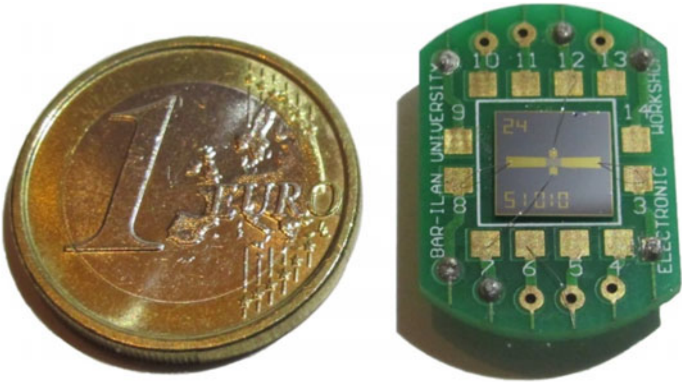

Fig. 13 A 5 mm PHE sensor mounted on its carrier, placed next to 1 EURO coin for scale

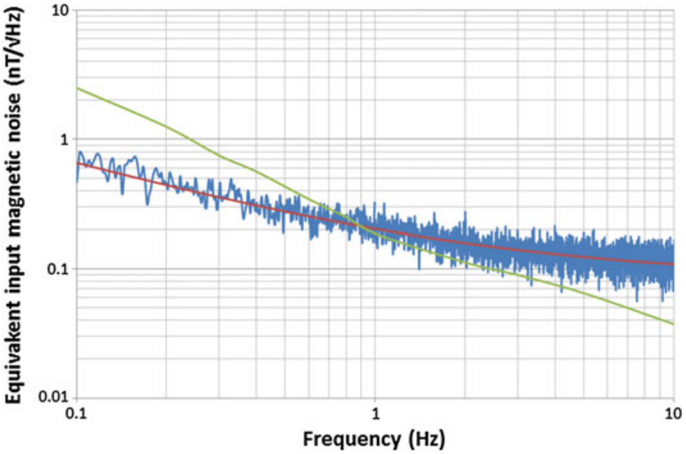

Fig. 14 The equivalent magnetic noise of a 5 mm elliptical PHE sensor (*blue line*—measured noise, *red line*—fit) compared to the equivalent magnetic noise of a high-resolution commercial AMR sensor of a model HMC1001 by Honeywell (*green line*)

conditions. We note that Eq. (26) equivalent magnetic noise is proportional to $\sqrt{H_{ea}}$.

The amplification of the field is commonly achieved by using magnetic flux concentrators. In the case of elliptical PHE sensors the integration of such concentrators is relatively simple. We note that flux concentrators have been used to increase the applied field by more than an order of magnitude.

The decrease of the noise can be achieved in several ways: by optimizing the sensor geometrical parameters including the parameters of the current and voltage leads and by optimizing the measuring method (amplitude and frequency of the excitation current, amplification circuit, etc.). Based on the above, even without exploring other material systems, a low frequency femto-Tesla resolution with the elliptical PHE sensors is within reach. In addition to the field resolution advantage of these sensors, there are other important advantages. They are simpler than the AMR sensors, their anisotropy is tailored by shape which enables the simple fabrication on the same chip of sensors with easy axes which differ in their orientation and the strength of the effective anisotropy field. Furthermore, they are quite robust and stable, a feature which decreases considerably the need to "refresh" the sensor. These features of the sensors make them suitable for a wide range of applications. They may compete with the low-cost low-resolution magnetic sensors such as Hall

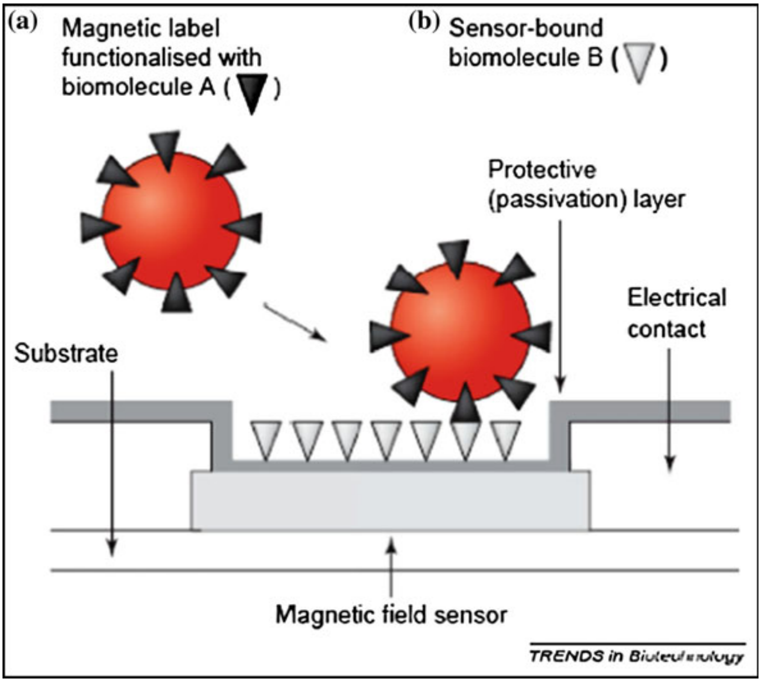

Fig. 15 Simplified scheme for biomolecule detection. Biomolecule with label (*A*) connecting to the sensing surface by creating a bridge with a complementary biomolecule (*B*). This event can be registered with a magnetic field sensor. Figure taken from [52]

sensors, which are widely used in the automotive industry. Currently, it appears that this industry does not need the improved resolution; however, it could be that once cheap, high-resolution sensors are available, the need will also arise.

PHE sensors have been suggested for various medical diagnostic applications; particularly, as a central part in lab-on-a-chip systems [52] (see Fig. 15). In such systems, better resolution means more sensitive diagnosis. Thus the use of elliptical PHE sensors in such systems may have important medical benefits. Furthermore, they can also become relevant for detecting magnetic fields generated by the human body in connection with heart and neural activity.

Another important field of application is related to magnetic anomaly detection of ferrous objects (for example: vehicles, submarines, etc.) The possible mass production of PHE sensors make them relevant for smart-dust [53] applications which require the distribution of a large number of sensors.

References

1. S.A. Wolf, A.Y. Chtchelkanova, D.M. Treger, Spintronics—a retrospective and perspective. IBM J. Res. Dev. **50**, 101–110 (2006)
2. S.A. Wolf, D.D. Awschalom, R.A. Buhrman, J.M. Daughton, S. von Molnár, M.L. Roukes et al., Spintronics: a spin-based electronics vision for the future. Science **294**, 1488–1495 (2001)
3. F.G. West, Rotating-field technique for galvanomagnetic measurements. J. Appl. Phys. **34**, 1171–1173 (1963)
4. C. Goldberg, R.E. Davis, New galvanomagnetic effect. Phys. Rev. **94**, 1121–1125 (1954)
5. T.T. Chen, V.A. Marsocci, Planar magnetoresistivity and planar hall effect measurements in nickel single-crystal thin films. Physica **59**, 498–509 (1972)
6. H.X. Tang, R.K. Kawakami, D.D. Awschalom, M.L. Roukes, Giant planar hall effect in epitaxial (Ga, Mn) as devices. Phys. Rev. Lett. **90**, 107201 (2003)
7. Y. Bason, L. Klein, J.B. Yau, X. Hong, C.H. Ahn, Giant planar hall effect in colossal magnetoresistive La0.84Sr0.16MnO3 thin films. Appl. Phys. Lett. **84**, 2593–2595 (2004)
8. X.S. Jin, R. Ramos, Y. Zhou, C. McEvoy, I.V. Shvets, Planar hall effect in magnetite (100) films. J. Appl. Phys. **99**, 08C509 (2006)
9. A.D. Henriksen, B.T. Dalslet, D.H. Skieller, K.H. Lee, F. Okkels, M.F. Hansen, Planar hall effect bridge magnetic field sensors. Appl. Phys. Lett. **97**, 013507 (2010)
10. A. Persson, R.S. Bejhed, F.W. Osterberg, K. Gunnarsson, H. Nguyen, G. Rizzi et al., Modelling and design of planar hall effect bridge sensors for low-frequency applications. Sens. Actuat. a-Phys. **189**, 459–465 (2013)
11. F.W. Osterberg, G. Rizzi, M.F. Hansen, On-chip measurements of Brownian relaxation of magnetic beads with diameters from 10 nm to 250 nm. J. Appl. Phys. **113**, 154507 (2013)
12. A. Persson, R.S. Bejhed, H. Nguyen, K. Gunnarsson, B.T. Dalslet, F.W. Osterberg et al., Low-frequency noise in planar hall effect bridge sensors. Sens. Actuat. a-Phys. **171**, 212–218 (2011)
13. S.J. Oh, T.T. Le, G.W. Kim, C. Kim, Size effect on NiFe/Cu/NiFe/IrMn spin-valve structure for an array of PHR sensor element. Phys. Status Solidi A **204**, 4075–4078 (2007)
14. N.T. Thanh, K.W. Kim, O. Kim, K.H. Shin, C.G. Kim, Microbeads detection using planar hall effect in spin-valve structure. J. Magn. Magn. Mater. **316**, E238–E241 (2007)

15. B. Bajaj, N.T. Thanh, C.G. Kim, in *Planar Hall Effect in Spin Valve Structure for DNA Detection Immobilized with Single Magnetic Bead.* 7th IEEE Conference on Nanotechnology, vol. 1–3 (2007), pp. 1037–1040
16. N.T. Thanh, B.P. Rao, N.H. Duc, C. Kim, Planar hall resistance sensor for biochip application. Phys. Status Solidi A **204**, 4053–4057 (2007)
17. S. Oh, N.S. Baek, S.D. Jung, M.A. Chung, T.Q. Hung, S. Anandakumar et al., Selective binding and detection of magnetic labels using PHR sensor via photoresist micro-wells. J. Nanosci. Nanotechno. **11**, 4452–4456 (2011)
18. D.T. Bui, M.D. Tran, H.D. Nguyen, H.B. Nguyen, High-sensitivity planar hall sensor based on simple gaint magneto resistance NiFe/Cu/NiFe structure for biochip application. Adv. Nat. Sci, Nanosci. Nanotechnol. **4**, 015017 (2013)
19. M. Volmer, J. Neamtu, Micromagnetic characterization of a rotation sensor based on the planar hall effect. Phys. B **403**, 350–353 (2008)
20. M. Volmer, M. Avram, A.M. Avram, in *On Manipulation and Detection of Biomolecules Using Magnetic Carriers*. International Semiconductor Conference (2009), pp. 155–8
21. T.Q. Hung, S.J. Oh, B.D. Tu, N.H. Duc, L.V. Phong, S. AnandaKumar et al., Sensitivity dependence of the planar hall effect sensor on the free layer of the spin-valve structure. IEEE Trans. Magn. **45**, 2374–2377 (2009)
22. T.Q. Hung, J.R. Jeong, D.Y. Kim, H.D. Nguyen, C. Kim, Hybrid planar hall-magnetoresistance sensor based on tilted cross-junction. J. Phys. D Appl. Phys. **42**, 055007 (2009)
23. B.D. Tu, L.V. Cuong, T.Q. Hung, D.T.H. Giang, T.M. Danh, N.H. Duc et al., Optimization of spin-valve structure NiFe/Cu/NiFe/IrMn for planar hall effect based biochips. IEEE Trans. Magn. **45**, 2378–2382 (2009)
24. B. Sinha, S. Anandakumar, S. Oh, C. Kim, Micro-magnetometry for susceptibility measurement of superparamagnetic single bead. Sens. Actuat. a-Phys. **182**, 34–40 (2012)
25. M. Volmer, J. Neamtu, Electrical and micromagnetic characterization of rotation sensors made from permalloy multilayered thin films. J. Magn. Magn. Mater. **322**, 1631–1634 (2010)
26. M. Volmer, J. Neamtu, Magnetic field sensors based on permalloy multilayers and nanogranular films. J. Magn. Magn. Mater. **316**, E265–E268 (2007)
27. T.Q. Hung, B.P. Rao, C. Kim, Planar hall effect in biosensor with a tilted angle of the cross-junction. J. Magn. Magn. Mater. **321**, 3839–3841 (2009)
28. Z.Q. Lu, G. Pan, Spin valves with spin-engineered domain-biasing scheme. Appl. Phys. Lett. **82**, 4107–4109 (2003)
29. B.D. Tu, L.V. Cuong, T.H.G. Do, T.M. Danh, N.H. Duc, Optimization of planar hall effect sensor for magnetic bead detection using spin-valve NiFe/Cu/NiFe/IrMn structures. J. Phys. Conf. Ser. **187**, 012056 (2009)
30. T.Q. Hung, S. Oh, J.R. Jeong, C. Kim, Spin-valve planar hall sensor for single bead detection. Sens. Actuat. a-Phys. **157**, 42–46 (2010)
31. M. Volmer, J. Neamtu, Optimisation of spin-valve planar hall effect sensors for low field measurements. IEEE Trans. Magn. **48**, 1577–1580 (2012)
32. K.M. Chui, A.O. Adeyeye, M.H. Li, Detection of a single magnetic dot using a planar hall sensor. J. Magn. Magn. Mater. **310**, E992–E993 (2007)
33. M. Volmer, J. Neamtu, in *Micromagnetic Analysis and Development of High Sensitivity Spin-valve Magnetic S*ensors. 5th International Workshop on Multi-Rate Processes and Hysteresis, vol. 268 (Murphys, 2010)
34. C. Christides, S. Stavroyiannis, D. Niarchos, Enhanced planar hall voltage changes measured in Co/Cu multilayers and Co films with square shapes. J. Phys. Condens. Mat. **9**, 7281–7290 (1997)
35. K.M. Chui, A.O. Adeyeye, M.H. Li, Effect of seed layer on the sensitivity of exchange biased planar hall sensor. Sens. Actuat. a-Phys. **141**, 282–287 (2008)
36. T.Q. Hung, S. Oh, B. Sinha, J.R. Jeong, D.Y. Kim, C. Kim, High field-sensitivity planar hall sensor based on NiFe/Cu/IrMn trilayer structure. J. Appl. Phys. **107**, 09E715 (2010)

37. F.W. Osterberg, G. Rizzi, T.Z.G. de la Torre, M. Stromberg, M. Stromme, P. Svedlindh et al., Measurements of Brownian relaxation of magnetic nanobeads using planar hall effect bridge sensors. Biosens. Bioelectron. **40**, 147–152 (2013)
38. S. Oh, S. Anandakumar, C. Lee, K.W. Kim, B. Lim, C. Kim, Analytes kinetics in lateral flow membrane analyzed by cTnI monitoring using magnetic method. Sens. Actuat. B-Chem. **160**, 747–752 (2011)
39. S. Oh, P.B. Patil, T.Q. Hung, B. Lim, M. Takahashi, D.Y. Kim et al., Hybrid AMR/PHR ring sensor. Solid State Commun. **151**, 1248–1251 (2011)
40. F. Qejvanaj, M. Zubair, A. Persson, S.M. Mohseni, V. Fallahi, S.R. Sani et al., Thick double-biased IrMn/NiFe/IrMn planar hall effect bridge sensors. Magn. IEEE Trans. **50**, 1–4 (2014)
41. F.W. Osterberg, A.D. Henriksen, G. Rizzi, M.F. Hansen, Comment on “Planar Hall resistance ring sensor based on NiFe/Cu/IrMn trilayer structure” [J. Appl. Phys. 113, 063903 (2013)], J. Appl. Phys. **114** (2013)
42. B. Sinha, T. Quang Hung, T. Sri Ramulu, S. Oh, K. Kim, D.-Y. Kim, et al., Planar hall resistance ring sensor based on NiFe/Cu/IrMn trilayer structure. J. Appl. Phys. **113**, 063903 (2013)
43. V. Mor, M. Schultz, O. Sinwani, A. Grosz, E. Paperno, L. Klein, Planar hall effect sensors with shape-induced effective single domain behavior. J. Appl. Phys. **111**, 07E519 (2012)
44. T. Musha, Physical background of Hooge’s α for 1/f noise. Phys. Rev. B **26**, 1042–1043 (1982)
45. M.A.M. Gijs, J.B. Giesbers, P. Beliën, J.W. van Est, J. Briaire, L.K.J. Vandamme, 1/f noise in magnetic Ni80Fe20 single layers and Ni80Fe20/Cu multilayers. J. Magn. Magn. Mater. **165**, 360–362 (1997)
46. J.A. Osborn, Demagnetizing factors of the general ellipsoid. Phys. Rev. **67**, 351–357 (1945)
47. C. Tannous, J. Gieraltowski, A Stoner-Wohlfarth model redux: static properties. Phys. B **403**, 3563–3570 (2008)
48. M.D. Donahue, D. Porter, OOMMF. http://math.nist.gov/oommf/
49. C.C. Chang, Y.C. Chang, W.S. Chung, J.C. Wu, Z.H. Wei, M.F. Lai et al., Influences of the aspect ratio and film thickness on switching properties of elliptical permalloy elements. Magn. IEEE Trans. **41**, 947–949 (2005)
50. A. Grosz, V. Mor, E. Paperno, S. Amrusi, I. Faivinov, M. Schultz, et al., Planar hall effect sensors with subnanotesla resolution. IEEE Magn. Lett. **4**, 6500104 (2013)
51. A. Grosz, V. Mor, S. Amrusi, I. Faivinov, E. Paperno, L. Klein, A high resolution planar hall effect magnetometer for ultra-low frequencies. IEEE Sensors J. **16**, 3224–3230 (2016)
52. D. Grieshaber, R. MacKenzie, J. Voros, E. Reimhult, Electrochemical biosensors—sensor principles and architectures. Sens. Basel **8**, 1400–1458 (2008)
53. J.M. Kahn, R.H. Katz, K.S.J. Pister, Emerging challenges: mobile networking for smart dust. Commun. Netw. J. **2**, 188–196 (2000)